Wideband Communication with Batteryless Sensors Embedded in Metal Structures

PETER OPPERMANN, Institute for Autonomous Cyber-Physical Systems, Hamburg University of Technology, Hamburg, Germany
BERND-CHRISTIAN RENNER, Institute of Autonomous Cyber-Physical Systems, Hamburg University of Technology, Hamburg, Germany

Structural health monitoring and predictive maintenance promise to significantly reduce costs, increase availability, and improve safety of civil infrastructure and industrial facilities. Wireless and batteryless sensors fuel these applications with the required data. As metal structures often shield sensor nodes from electromagnetic waves, acoustic power and data transfer are promising alternatives. However, the metal channel suffers from severe multipath propagation, limiting data rates to typically less than 200 $\text{bit}\,\text{s}^{-1}$. We investigate wideband pulses as alternative to commonly used continuous wave modulation schemes to increase robustness. In a simulation study, we first compare wideband modulation with narrowband modulation schemes and assess their robustness against noise and clock deviations. We then construct a wirelessly powered tag prototype to validate the simulation results in real-world metal channels. Furthermore, we propose a reader-based synchronization scheme to mitigate clock mismatch, which is inevitable with ultra-low-power tags. The results show that wideband pulse-position modulation is the most favorable modulation scheme, increasing the median data rates in many scenarios by 132 % over continuous-wave schemes. Additionally, wideband pulses are advantageous for power transfer in the highly frequency-selective channel when optimal carrier frequencies are yet unknown. However, simultaneous power transfer and communication on the same transducer are shown to interfere with each other, complicating the receiver design.

CCS Concepts: • **Computer systems organization → Sensor networks**; • **Hardware → Wireless devices;**

Additional Key Words and Phrases: Acoustic, through-metal communication, backscatter, downlink, wireless power transfer

ACM Reference Format:
Peter Oppermann and Bernd-Christian Renner. 2025. Wideband Communication with Batteryless Sensors Embedded in Metal Structures. *ACM Trans. Internet Things* 6, 3, Article 20 (August 2025), 27 pages. https://doi.org/10.1145/3748517

1 Introduction

Maintenance and repair of aging infrastructure is a significant cost factor in many industrialized countries [10]. Automated Structural Health Monitoring (SHM) enables the detection of structural

---

Authors' Contact Information: Peter Oppermann, Institute for Autonomous Cyber-Physical Systems, Hamburg University of Technology, Hamburg, Hamburg, Germany; e-mail: peter.oppermann@tuhh.de; Bernd-Christian Renner, Institute of Autonomous Cyber-Physical Systems, Hamburg University of Technology, Hamburg, Germany; e-mail: christian.renner@tuhh.de.

ACM 2577-6207/2025/08-ART20
https://doi.org/10.1145/3748517

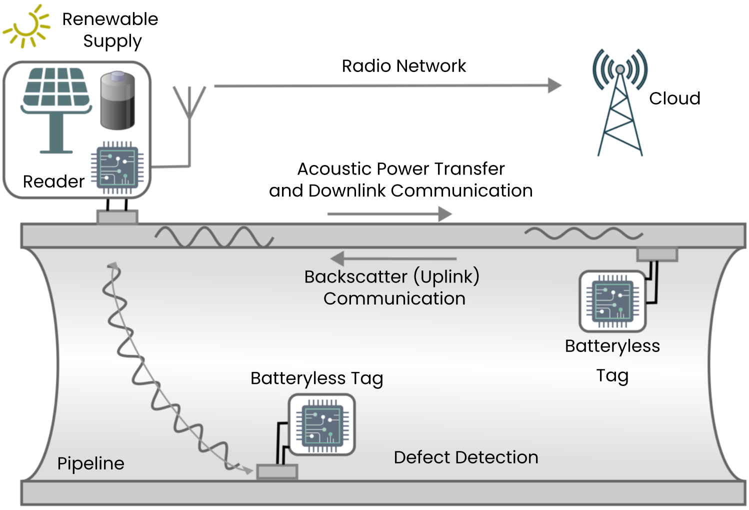

Fig. 1. Pipeline monitoring is an application for batteryless sensors requiring through-metal communication, as regular battery swaps are difficult and costly.

damages early—when repair is often simple and cheap. SHM may also enable predictive maintenance, reducing costly and time-consuming manual inspections in favor of dynamic checkups tailored to a structure's specific damage risk. However, collecting the necessary sensory data is still challenging: Typical structures, e.g., bridges or pipelines, are often large, requiring the distribution of hundreds to thousands of sensors [17]. Small, affordable, low-maintenance sensors are therefore essential for cost-effective SHM, making batteryless wireless sensors the preferred choice [6]. Figure 1 sketches an exemplary application for batteryless pipeline monitoring, where post-deployment battery replacement is especially cumbersome.

A prominent example of batteryless devices is computational Radio-Frequency Identification (RFID) [31], which achieves ultra-low-power communication and wirelessly powered sensors with radio frequencies. However, many locations on structures are shielded by metal, where electromagnetic waves are impractical due to strong attenuation [30]. In such scenarios, acoustic power transfer and communication with passive batteryless sensors through metal structures are a promising alternative [23, 27, 28]. First, an active readout device (reader) generates a carrier waveform, wirelessly powering a passive sensor device (tag). Furthermore, the tags use backscatter communication to transmit (sensor) data by modulating the reflection of the incident carrier, achieving communication at ultra-low-power consumption.

Because they act as waveguides with little attenuation, plate-like metal structures support efficient power transfer and wireless communication over long distances [19]. Unfortunately, the existing approaches to guided-wave communication suffer from a major drawback: Strong multipath-propagation leads to Inter-Symbol Interference (ISI), often limiting data rates to only 20 bits^{-1} to 200 bits^{-1}.

Although typical SHM applications may not require transmitting large amounts of data, high data rates are still favorable: they reduce power-consuming active times of the passive tags and enable a single reader to serve multiple tags by time-division multiple access. In previous work, we have shown that the data rates for the tag-to-reader communication (uplink) can be increased significantly by implementing higher-order modulation schemes or equalizers in the receiver [18, 20]. However, this requires considerable computational resources on the receiving side, and, hence, is infeasible for the inverse direction from the reader to the tag (downlink): The tags must work with a restrictive energy budget and can neither implement complex filters and receiver structures, nor use high sampling rates.

Our goal is to elevate the downlink data rate into the kilobit-per-second range while preserving the tag's ultra-low complexity and energy efficiency. Because the tag is wirelessly powered, its energy consumption directly affects its activation range. Inspired by the WISP open-source RFID platform [22], we target sub-milliwatt power consumption during active operation and a minimum startup threshold of approximately 0dBm. These specifications would allow wireless activation at distances exceeding ten meters in metal structures [19], assuming a reader transmitting at 1 W—the power limit permitted for commercial RFID devices.

1.1 Contributions and Article Organization

This work proposes wideband modulation to enhance downlink data rates. It shifts the computational burden of ISI mitigation and synchronization to the more powerful reader. We construct a reader that generates wideband pulses, which outperform continuous-wave (CW) modulation schemes in multipath-resistance. At the same time, we avoid increasing tag complexity by reusing simple and energy-efficient amplitude demodulation schemes. In particular, we

- perform a simulation study comparing common Continuous Wave (CW) modulation schemes with the proposed wideband modulation in four channels recorded from a real specimen,
- design a tag and reader prototype to validate the simulation results and assess practical limitations due to frequency offsets,
- propose a reader-centered synchronization scheme to mitigate the effect of Sampling Frequency Offset (SFO) at the tag,
- analyze the interdependence between power transfer and communication over the same transducer, showing that the tag requires fine-grained control over the energy harvester, and
- publish the source code of the simulation and schematics and PCB layout of the tag prototype under an open-source license, which we detail in Section A.

The following section reviews the related work in low-power acoustic communication and wirelessly power transfer through metals and demonstrates why established techniques, e.g., from RFID, are unsuitable for acoustic communication. The remainder of the article is structured in two main parts, aligned with the research methodology. Section 3 and Section 4 develop and evaluate the proposed communication scheme through simulation, identifying key design choices and tradeoffs. Section 5 and Section 6 then describe the hardware implementation of a prototype tag and evaluate it experimentally, demonstrating the feasibility of the approach under real world conditions in a realistic metal environment. Finally, Section 7 discusses the broader insights and future challenges, and Section 8 concludes the work.

2 Related Work

This section reviews acoustic communication and Wireless Power Transfer (WPT) for batteryless and ultra-low-power sensor nodes in metal. We also compare strategies from adjacent domains, dealing with similarly constraints. Because harvestable power declines rapidly with distance, passive tags must operate on sub-milliwatt power budgets. This imposes severe resource constraints.

2.1 Through-metal Communication

Through-metal communication techniques differ widely in terms of channel characteristics and receiver complexity. Most prior studies target channels with coaxially aligned transducers placed on opposing sides of a metal barrier, a setup often referred to as Sandwich-Plated (SWP)

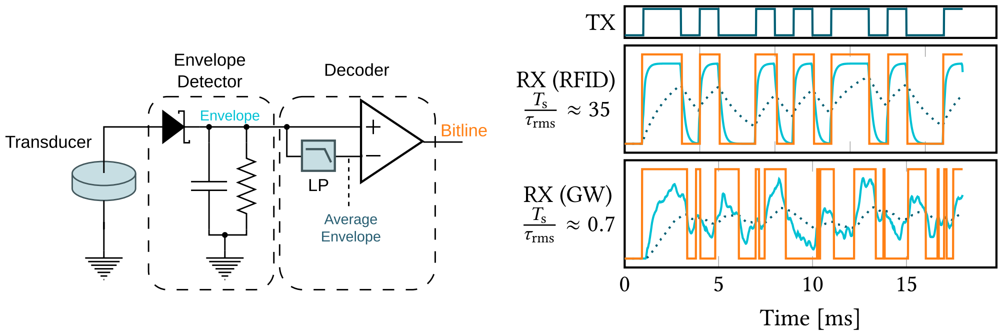

(a) (b)

Fig. 2. Conventionally used diode-based envelope detector (a) with a subsequent decoder generating a bitline from the passband signal at variable carrier frequencies. Performance degradation (b) when channel delay spread τ_{rms} and T_{s} are in the same order of magnitude.

channel. In these configurations, longitudinal waves in the megahertz frequency range are employed, enabling data rates up to 30 kbits^{-1} with simple receivers [3, 8, 24], and up to 17 Mbits^{-1} with complex, power-intensive OFDM receivers [13]. However, the reliance on strict coaxial alignment and the strong attenuation of longitudinal waves restrict the transmission range to a few centimeters.

An alternative approach uses Guided Wave (GW) in plate-like metal structures. GWs propagate efficiently through the structure with attenuation as little as 1 dB m^{-1} [26], enabling communication over distances of several tens of meters. Consequently, this work focuses on GW channels.

Given the resource constraints of passive tags, complex receivers are impractical. Instead, simple diode-based envelope detectors (ED) (Figure 2(a)) are widely used for demodulating signals in through-metal [28], underwater [12], and RFID systems [22, 31]. An ED typically consists of a low-pass filter that averages the signal envelope across multiple symbol periods, and is followed by a comparator that detects whether the instantaneous envelope exceeds the average. This architecture can generate a digital bitline with minimal, low-cost, energy-efficient components, requiring only simple digital logic for decoding. However, because phase and frequency information are lost during envelope detection, only amplitude modulation schemes are feasible.

Despite their low attenuation, GW channels introduce challenges. Chief among them is severe multipath propagation: strong reflections at metal-air boundaries cause extended reverberation and ISI. Our previous work demonstrated RMS channel delay spreads up to 2 ms in meter-scale metal beams, limiting ISI-free symbol rates under 200 bits^{-1} [19]. Figure 2(b) shows, how increasing ISI disrupts bitline recovery with a conventional ED receiver. When the symbol duration strongly exceeds the channel delay spread (as typical in RFID systems, where delay spreads are usually around 10 ns to 80 ns [2]), decoding is robust. In contrast, when the symbol duration is comparable to the delay spread, bitline reconstruction fails. Consequently, GW-based systems with low-complexity receivers must decrease the symbol rates to facilitate correct transmission. Accordingly, existing studies with low-power receivers achieved only modest data rates between 20 and 200 bits^{-1} [15, 28].

Table 1 summarizes prior studies on low-power GW communication. Notably, two studies adopt Binary Frequency-Shift Keying (BFSK) modulation, while retaining an ASK receiver, exploiting channel-induced amplitude differences at different frequencies [23, 28]. While effective, these

Table 1. Comparison of the Existing Studies about Low-power Acoustic Downlink Communication

Study	**Spec.**	**Distance** m	**Freq.** kHz	**Modul.**	**Data rate bits^{-1}**	**Impl. Level**
Tang, 2022 [28]	Plate	< 0.3	400	BFSK	200	CMOS IC
Shaik,2020 [23]	Plate	0.5	250	BFSK	80	AF^2 + MCU
Mijarez, 2013 [15]	Pipe	30	40	PPM	20	DSP
Chakraborty, 2015 [5]	Pipe	4.8	455	Chirp-OOK	100	AF^2 + MCU

Abbreviations: *Spec.*: Specimen, *Modul*: Modulation type, *BFSK*: Binary Frequency-Shift Keying, *PPM*: Pulse Position Modulation, *OOK*: On/Off Keying, *IC*: Integrated Circuit, *AF*: Custom Analog Frontend, *MCU*: Microcontroller, *DSP*: Digital Signal Processor.

methods achieve data rates below 200 bits^{-1} and operate over short ranges (< 1 m). Other approaches, such as Pulse-Position Modulation (PPM) and chirp-based On/Off-Keying (OOK), extend distances to up to 30 m but at very low data rates [5, 15].

Overall, the diversity in channel geometries, frequency ranges, transmission distances, and evaluation methodologies hinders direct comparison. Furthermore, all prior studies manually optimized the carrier frequency to match a specific channel, and neglected evaluations of system robustness against practical impairments such as clock mismatches between reader and tag, or ambient noise. This work systematically compares CW modulation schemes across multiple CW channels and introduces a novel wideband modulation method designed for improved robustness against multipath fading.

2.2 Through-metal Power Transfer

Power transfer typically involves introducing a CW acoustic carrier into the structure, which the tag's piezoelectric transducer converts into an AC voltage. After rectification, the resulting DC voltage is buffered in a storage capacitor to smooth out fluctuations. Given that harvested amplitudes often fall short of electronics supply requirements, voltage booster circuits are essential.

GW-based power transfer introduces two specific challenges: strong frequency-selectivity in channel gain and transducer impedance. First, the channel gain exhibits short resonances. Even minor frequency deviations (tens of Hertz) can cause gain variations exceeding 20 dB [19]. Moreover, transducer placement affects harvesting efficiency; standing wave patterns mean that sensors positioned at wave nodes receive orders of magnitude less energy than those at antinodes. Predicting the optimal frequency *a priori* is infeasible, given the sensitivity to structural geometry, temperature, stress, and transducer placement. While many studies manually tune the carrier frequency to maximize the transfer efficiency [27, 29], this approach is impractical for dynamic environments. Shaik et al. [23] partially addresses variability with a self-optimizing reader and tag pair that track slow variations of the optimal frequency over time. However, a suitable initial frequency has to be chosen manually.

Second, the tag transducer's output impedance in GW channels varies substantially with frequency, tightly coupled to the vibrational response of the structure. Variations by a factor of five within frequency changes of ten hertz are typical [18]. Matching the transducer impedance at the harvester is crucial for maximizing efficiency. WPT in adjacent fields, e.g., acoustic underwater [4] and in-body [11], assumes constant transducer impedance and employs a static matching circuit. In contrast, in GW-based methods, manual channel-specific matching for each tag can increase efficiency more than 40-fold e.g., [29]. Although Maximum Power-Point Tracking (MPPT) can dynamically adapt the harvester's input impedance, its variations distorts the envelope if the same transducer is used for harvesting and communication. We analyze these effects in Section 5.2.1.

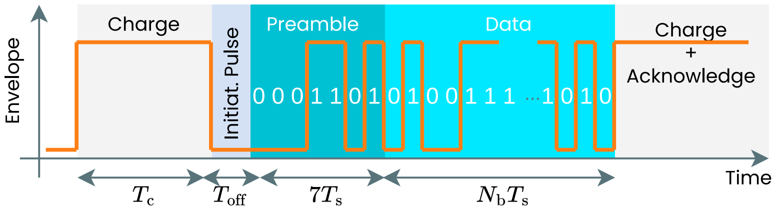

Fig. 3. The general message structure applies to all modulation schemes in this section. The signal in this example, encodes message and preamble bits in OOK.

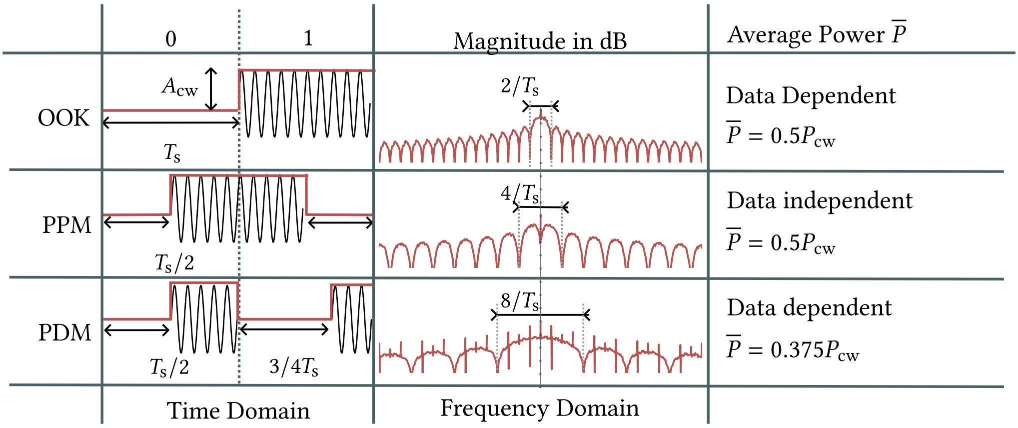

Fig. 4. Overview of the investigated CW modulation schemes and encodings, their magnitude spectrum, and their average signal power relative to the CW power P_{cw}.

3 System Design

This section describes the communication protocol and receiver design, focusing on the downlink from reader to tag. We introduce the narrowband modulation schemes selected for comparison—chosen for their prevalence in RFID and existing piezoacoustic backscatter systems—and then present a new wideband modulation approach.

3.1 Protocol and Modulation

Figure 3 illustrates the message structure common to all investigated modulation schemes. Our system adopts a *reader-talks-first* protocol, a strategy widely used in backscatter communications, including EPCGlobal RFID standards [9] and recent acoustic protocols [23].

In reader-talks first protocols, a downlink transmission proceeds as follows: Initially, the reader transmits a CW carrier to charge the passive tag. To minimize the tag's power consumption during idle periods, each downlink message begins with an *initialization pulse*, briefly interrupting the carrier for a time interval T_{off}. This pulse allows the tag to operate with a lower sampling rate instead of continuously correlating with a preamble, as evaluated in Section 6.4.

Following the initialization pulse, a 7-symbol barker sequence serves as preamble for frame synchronization. Subsequently, N_b data symbols are transmitted at symbol rate $1/T_s$. The number of symbols per message is application specific N_b and is analyzed in Section 4.2.3. Finally, the reader resumes the CW carrier to recharge the tag and facilitate backscatter-based acknowledgments in the uplink.

The modulation schemes under investigation are summarized in Figure 4. They are chosen to consider critical limitations of the resource-constrained tag:

- Avoiding power-hungry frequency mixing, signal demodulation relies solely on an envelope detector (ED), ruling out schemes based on phase or frequency modulation.
- No amplifier is available; harvested signals must be strong enough to detect without amplification.
- No active gain control is employed; excessive signal strength may saturate the ADC, causing signal distortion.
- Tags harvest energy continuously during reception, with available power depending on the modulation scheme.

To maximize simplicity and robustness, only binary modulation schemes are considered.

3.1.1 Continuous Wave Modulation. In Amplitude Modulation (AM), the carrier's amplitude alternates between two levels A_{cw} and A_{low} using rectangular pulses. A_{low} can be adjusted to balance average transferred power and SNR. Furthermore, if A_{low} is too high, the amplitude swing becomes small, making the signal susceptible to saturation at resonant frequencies. To avoid this risk, we set $A_{\text{low}} = 0\,\text{V}$.

Three different AM-based encodings are considered. In OOK, the carrier's amplitude is either zero or high throughout the whole symbol period, depending on the transmitted bit. However, during long sequences of zeros, the tag may not receive sufficient energy, risking energy depletion.[1] In PPM, a short pulse occupies either the first or second half of the symbol period, depending on the bit value. By setting the pulse width to $T_s/2$, we maintain a constant average power at half of the CW carrier's power. Lastly, in Pulse Duration Modulation (PDM), every symbol period ends with a high-level pulse whose duration varies according to the bit value. The average power depends on the data pattern but remains between $0.25P_{\text{cw}}$ and $0.5P_{\text{cw}}$.

3.1.2 Wideband Modulation. In contrast to the established CW modulation schemes, we propose a wideband pulse-based approach. Among the family of wideband methods—such as chirp spread-spectrum, direct-sequence spread-spectrum, and OFDM—short-duration pulses fit best with the resource-constrained tag receiver. Such pulses can be detected solely based on their envelope, eliminating the need for complex matched filters. We define a TX pulse $p_{\text{wb}}(t)$ in this regard as

$$p_{\text{wb}}(t) = A_{\text{wb}} \cos(2\pi f_c t)\,\text{sinc}(Bt)\,, \tag{1}$$

where A_{wb} is the peak amplitude of the pulse and B is the pulse's bandwidth. This pulse has a frequency spectrum of

$$\mathcal{F}\{p_{\text{wb}}\}(f) = \frac{A_{\text{wb}}}{2B}\text{rect}\left(\frac{|f| - f_c}{B}\right)\,, \tag{2}$$

where the signal energy is distributed equally over the specified bandwidth. The rectangular function $\text{rect}(f)$ equals one for all f between -0.5 and 0.5, and zero otherwise. For a fair comparison with the continuous wave modulation, we choose A_{wb} so that a wideband pulse has the same total energy as the rectangular CW pulses with amplitude A_{cw} and duration T_s, i.e.,

$$A_{\text{wb}} = A_{\text{cw}}\sqrt{T_s \cdot B}\,. \tag{3}$$

We further consider two encodings illustrated in Figure 5. Wideband OOK (WB-OOK) encodes a one-bit by the presence of a pulse during a symbol period, while a zero-bit is represented by the absence of a pulse. Similarly, in Wideband Pulse-Position Modulation

---

[1] Line coding, such as Manchester coding, could mitigate this effect, but would effectively transform the signal into a PPM equivalent.

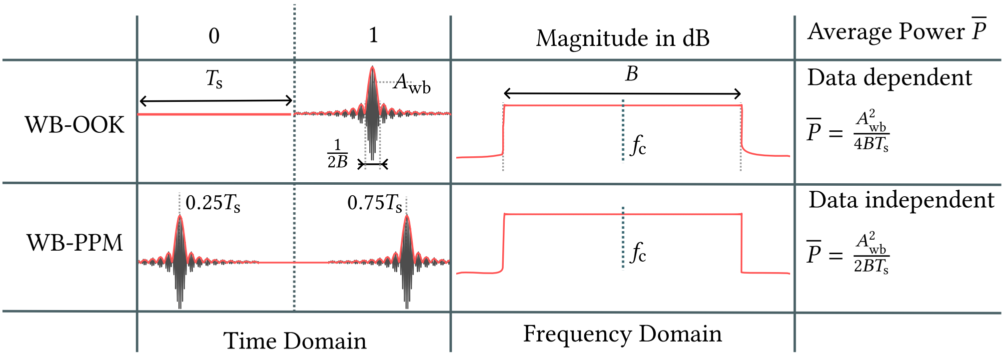

Fig. 5. The investigated wideband modulation schemes and encodings, their magnitude spectrum, and their average signal power.

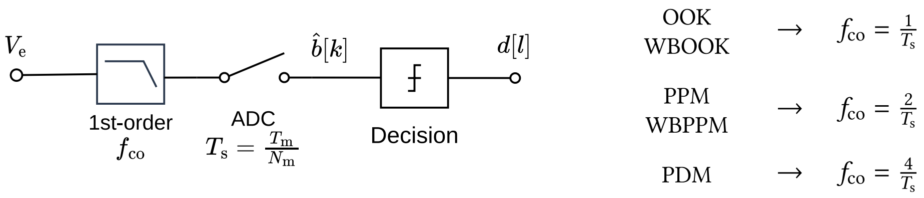

Fig. 6. The receiver is modeled by a passive RC-lowpass filter before sampling. The cutoff frequency is inversely proportional to each modulation scheme's shortest pulse duration, i.e., the main lobe's bandwidth.

(WB-PPM), the pulse is shifted in time to peak at $T_s/4$ or $3T_s/4$ to encode a one-bit and zero-bit, respectively. By adopting the amplitude normalization in Equation (3), WB-OOK and WB-PPM deliver the same average signal power to the tag as their narrowband counterparts (OOK and PPM).

3.2 Receiver Design

At the receiver, the incoming envelope signal V_e passes through a passive first-order lowpass filter. The cutoff frequency f_{co} is adapted to the signal's shortest pulse duration, as summarized in Figure 6. The filtered signal is then sampled at rate N_m/T_s.

Given the tag's resource constraints, the receiver architecture is deliberately simple and uses low sampling rates and no complex filters such as equalizers. Frame synchronization is achieved by correlating the sampled signal $\hat{b}[k]$ with the expected preamble sequence, yielding the start index k_0 of the first message symbol. The symbol decisions $d[l]$ for the lth symbol are subsequently made by correlating the received samples against ideal symbol templates, specific to the selected modulation and encoding.

For OOK and WB-OOK, the receiver compares the mean signal value throughout each symbol period to a dynamic threshold $\hat{b}_{th}$ initially estimated from the preamble samples. Due to long channel delay spreads, the effective threshold drifts with transmitted data sequences: falling after a run of zeros or rising after consecutive ones. Final bit decision are made as

$$d_{ook}[l] = \begin{cases} 0 & \text{if} \quad c > \hat{b}_{th} \\ 1 & \text{else} \end{cases} \quad \text{with} \quad c = \frac{1}{N_m} \sum_{i=0}^{N_m-1} \hat{b}[k_0 + lN_m + i]. \tag{4}$$

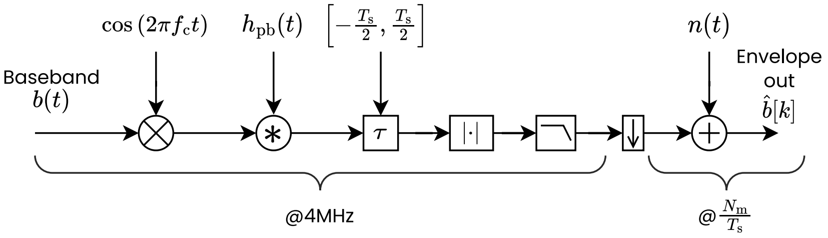

Fig. 7. Simulation signal flow. The input baseband signal is generated differently depending on the selected modulation and encoding scheme.

In contrast, PPM and WB-PPM require no absolute threshold. Instead, they compare the mean of the first and second half of each symbol independent of the absolute signal amplitude.

$$d_{\mathrm{ppm}}[l] = \begin{cases} 0 & \text{if} \quad c_1 - c_2 > 0 \\ 1 & \text{else} \end{cases} \quad \text{with}$$
$$c_1 = \sum_{i=0}^{N_m/2-1} \hat{b}[k_0 + lN_m + i] \quad \text{and} \quad c_2 = \sum_{i=N_m/2}^{N_m-1} \hat{b}[k_0 + lN_m + i] \tag{5}$$

Finally, for PDM, symbol decisions focus exclusively on samples within the interval $\mathcal{I}$—the pulse specific region that differs between zero and one symbols.

$$d_{\mathrm{pdm}}[l] = \begin{cases} 0 & \text{if} \quad c < \hat{b}_{\mathrm{th}} \\ 1 & \text{else} \end{cases} \quad \text{with} \quad c = \frac{1}{|\mathcal{I}|} \sum_{i \in \mathcal{I}} \hat{b}[k_0 + lN_m + i]. \tag{6}$$

4 Simulation Study and Evaluation

To evaluate the robustness of the proposed modulation schemes, we developed a simulation framework that models realistic downlink communication over metallic structures. The simulation examines performance under multipath propagation, frequency and timing offsets, and additive noise—conditions characteristic of real-world metal channels. Given that frequency-selectivity and variability of the GW channels are a key challenge, and channel characteristics vary significantly with geometry and transducer placement, we conducted impulse response measurements across four distinct physical channels. These recorded responses were used throughout the simulation to ensure simulated conditions are realistic and that our method is not tailored to only a single channel.

4.1 Simulation Setup

Figure 7 outlines the signal processing pipeline of our simulation. Starting from a pseudo-random bit sequence, the baseband signal $b(t)$ is modulated according to the selected scheme. The baseband is then upconverted to passband by mixing with the carrier frequency f_c and convolved with the channel impulse response $h_{pb}(t)$, sampled at 4 MHz—matching the resolution of our channel measurements.

To simulate the effects of unsynchronized clocks between reader and tag, a random timing offset is introduced, drawn uniformly from the range $[-T_s/2, T_s/2]$. An ideal envelope detector is modeled by computing the signal's absolute value and lowpass filtering it. Finally, the result is downsampled to the receiver's sampling rate, and Additive White Gaussian Noise (AWGN) is added.

To obtain real-world impulse responses, we mounted five piezoelectric transducers to a 3.5 m steel beam using epoxy resin. We examined four unique channels formed by varying the

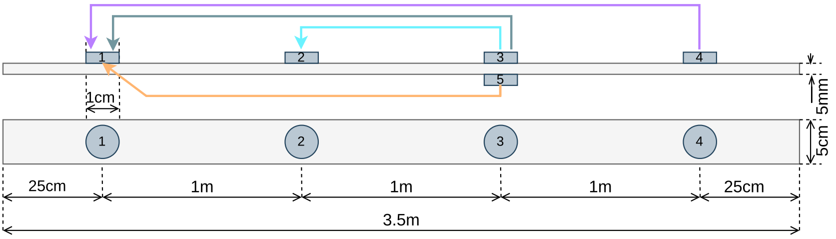

Fig. 8. The metal beam used for channel impulse response measurements and prototype evaluation. We selected four different pairs of transducers, yielding four different channels.

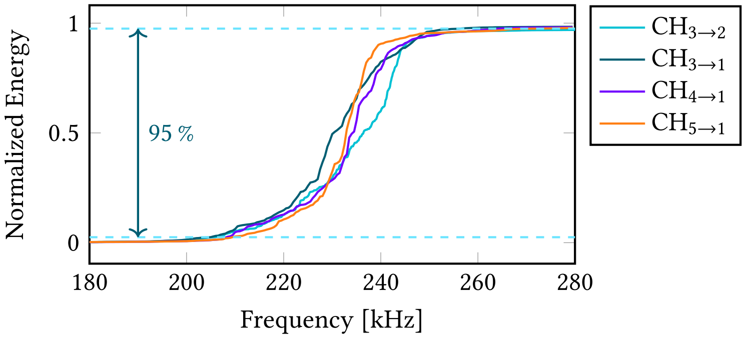

Fig. 9. Cumulative spectral energy of the impulse responses for four channels on the investigated specimen. More than 95 % of the energy is within 200 kHz to 250 kHz.

transmitter-receiver transducer pairs—ranging from 1 to 3 meters apart, and positioned either on the same or on opposite sides of the beam (Figure 8). We denote a specific channel as $\mathrm{CH}_{a\to b}$, where a specifies the transmitting transducer and b is the receiving transducer. Each transducer was a 1 cm, 2 mm thick piezoceramic disk with a nominal radial resonance frequency of 200 kHz.

Impulse responses were acquired using chirp-based channel sounding. A signal generator transmitted linear chirps of duration $T = 100$ ms and bandwidth $f_{\mathrm{max}} = 2$ MHz, while the response was recorded using a TiePie Handyscope HS-5 oscilloscope. The chirp signal is given by:

$$x_{\mathrm{chirp}}(t) = A_0 \sin\left(2\pi \int_0^t \frac{f_{\mathrm{max}} \cdot \tau}{T} d\tau\right), \tag{7}$$

where A_0 is the signal amplitude. Chirps are widely used in acoustic measurements due to their flat frequency response and constant amplitude, which helps prevent distortion from amplifier saturation and distributes energy uniformly over time [25].

The impulse response $h_{\mathrm{pb}}(t)$ is computed via frequency-domain deconvolution:

$$h_{\mathrm{pb}}(t) = \mathcal{F}^{-1}\left\{\frac{\mathcal{F}\{y_{\mathrm{chirp}}\}}{\mathcal{F}\{x_{\mathrm{chirp}}\}}\right\}, \tag{8}$$

where $y_{\mathrm{chirp}}(t)$ is the received signal.

To optimize the wideband pulse design, we analyzed the frequency content of the impulse responses. In all four channels, over 95 % of the signal power was concentrated between 200 kHz and 250 kHz, as shown by the cumulative spectral energy density in Figure 9. Based on this, we selected a wideband pulse with center frequency $f_c = 225$ kHz and bandwidth $B = 50$ kHz for all subsequent simulations.

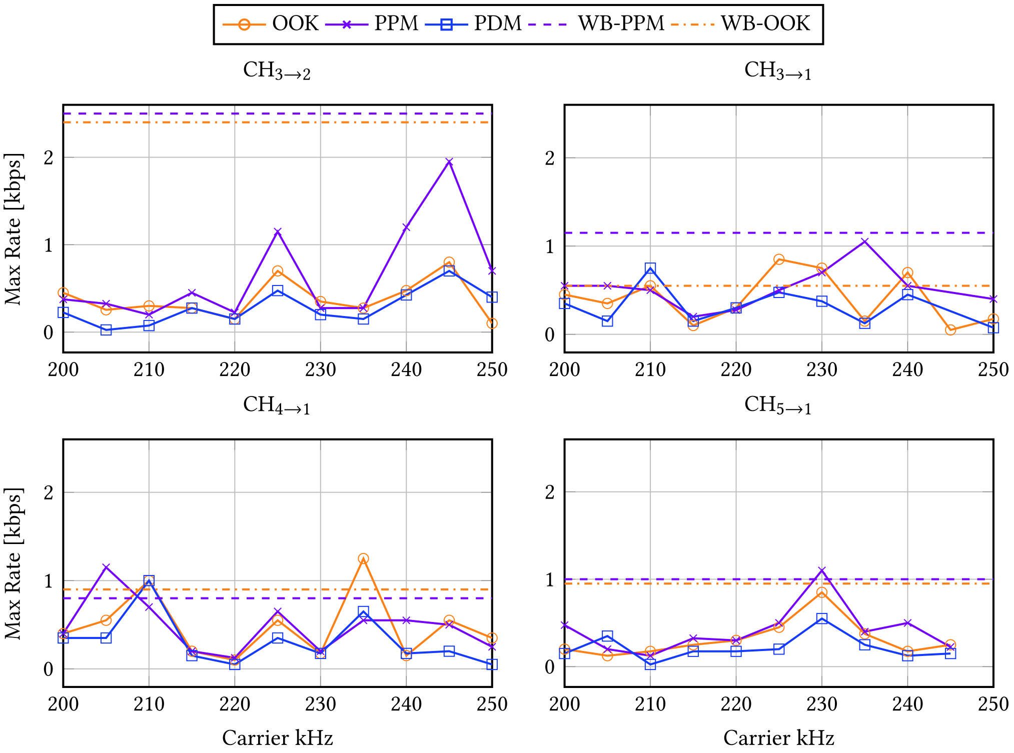

Fig. 10. The highest achievable data rates that supported a BER below 10^{-5} in simulation for all modulation schemes.

4.2 Simulation Results

4.2.1 Achievable Data Rates. We used the channel simulation to estimate the maximum achievable data rates for each modulation scheme. For narrowband CW schemes, whose error rates depend strongly on carrier frequency, we evaluated 11 evenly spaced carrier frequencies from 200 kHz to 250 kHz across the four measured channels ($CH_{3\to2}$, $CH_{3\to1}$, $CH_{4\to1}$, and $CH_{5\to1}$). In each case, we began at a nominal rate of 3 bits^{-1} and progressively reduced the rate in 50 bits^{-1} increments until the bit error rate (BER) dropped below 10^{-5} across ten thousand messages of 100 bits each— totaling 10^6 transmitted bits. In this experiments, we used a noise standard distribution $\sigma = 10\,\text{mV}$, roughly corresponding to noise observations at the prototype's ADC. Furthermore, we chose $N_\text{m} = 10$.

Unlike CW schemes, wideband modulations inherently occupy the full target bandwidth, and are thus evaluated at a single center frequency per channel. The resulting data rates are summarized in Figure 10.

Three key insights emerge from the narrowband results:

(1) Data rate varies significantly with carrier frequency—by more than an order of magnitude between optimal and suboptimal frequencies.
(2) The *best* frequency is not consistent across channels; channel-specific resonance characteristics dominate performance.
(3) At any given frequency, the performance gap between modulation schemes can be substantial, though no scheme clearly outperforms the others in all scenarios.

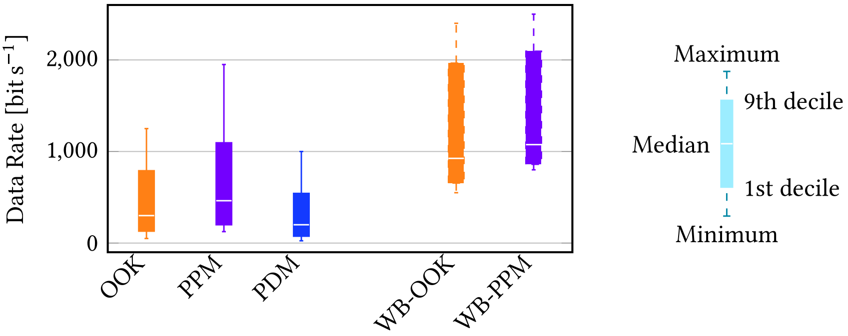

Fig. 11. The distribution of the achieved data rates with the narrowband modulation schemes at various carrier frequencies and the wideband schemes in multiple channels. The notation of the boxplot is visualized on the right.

Figure 11 captures the distribution of achievable narrowband rates across all settings. Among these, PPM offers the most consistent throughput, while PDM generally trails behind.

In contrast, wideband modulation consistently delivers a more reliable data rate in all four channels. In channel $CH_{3\rightarrow 2}$, they exceed the maximum narrowband rates considerably with up to 2,500 bits^{-1} compared to 1,950 bits^{-1} with PPM at $f_c = 245$ kHz. In channel $CH_{3\rightarrow 1}$, WB-PPM is nearly identical with the fastest narrowband option at 1100 bits^{-1}. In $CH_{4\rightarrow 1}$, WB-OOK is about 30 % below the maximum narrowband channel, yet still well above the average throughout all carrier frequencies. Finally, in channel $CH_{5\rightarrow 1}$, the WB-PPM is 10 % below the fastest narrowband scheme. In all cases, even in the 3 m long channel $CH_{4\rightarrow 1}$, which supports the lowest throughput, the observed data rates of WB-PPM are still above 800 bits^{-1}, with a median of 1075 bits^{-1}—a 132 % increase over the median of the fastest narrowband scheme.

There results indicate that, in the absence of channel-specific tuning, wideband modulation—particularly WB-PPM—offers greater reliability and more predictable data rates than narrowband alternatives. Accordingly, the remainder of this study focuses on analyzing the influence of different parameters for WB-PPM.

4.2.2 Samples Per Symbol.

The number of samples per symbol (N_m) represents a critical tradeoff between decoding reliability and the tag's computational load. While fewer samples reduce power consumption and processing complexity—essential in ultra-low-power systems—they can compromise decoding accuracy. To evaluate this tradeoff for wideband modulation schemes, we repeated the channel simulations with varying sampling rates.

As shown in Figure 12, using $N_m = 10$ provides a balanced compromise: it ensures reliable decoding without imposing excessive computational demands. Reducing the sampling rate to six samples per symbol leads to a sharp performance decline—bit error rates rise by up to two orders of magnitude, and achievable data rates drop by nearly 50 %. Conversely, even doubling the rate to 20 samples yields only marginal improvements in error performance, with no measurable gain in data throughput.

Results for the two additional channels, which exhibit similar trends, are omitted here for brevity.

4.2.3 Impact of Sampling Frequency Offset.

Clocks in low-power microcontrollers often deviate up to 1 % from their nominal frequency, as specified in device datasheets. Moreover, clock rates are sensitive to ambient temperature and supply voltage fluctuations [19]. These variations introduce SFO, potentially causing the transmitter and receiver to drift out of synchronization during a message. While tracking and correcting SFO during reception is possible, doing so on

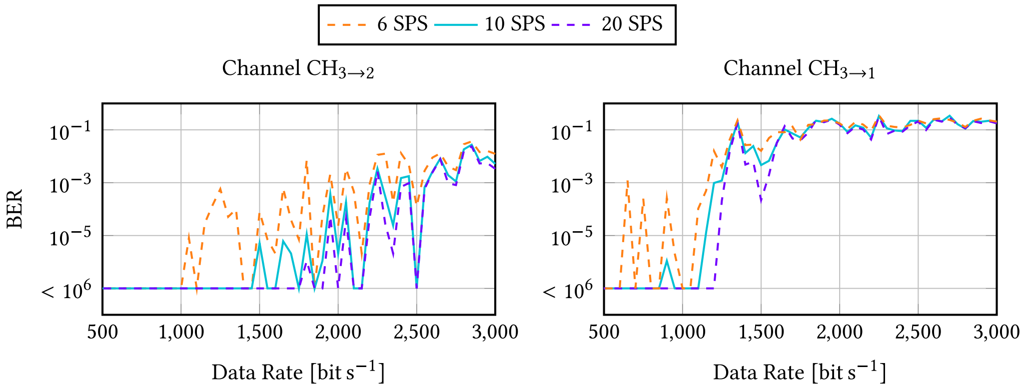

Fig. 12. Influence of the number of symbols on the BER for the WB-PPM modulation scheme.

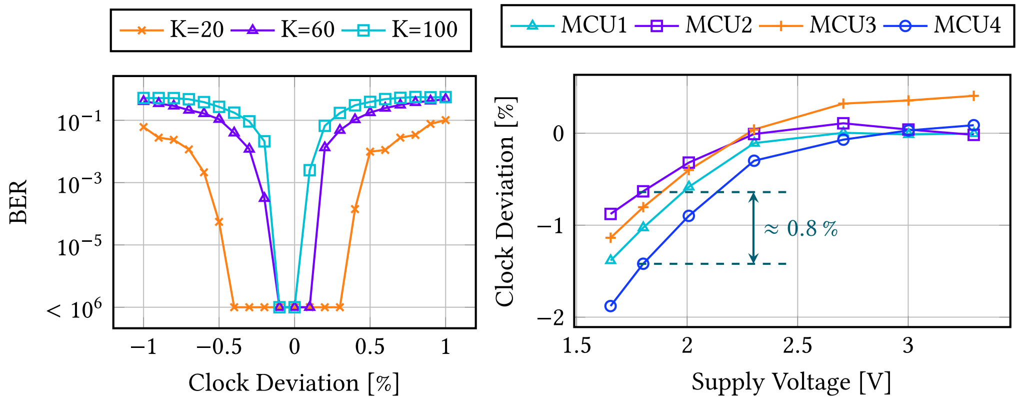

Fig. 13. The influence of MCU clock deviation on the BER depending on the message length (left). Typical clock deviation in multiple devices from the same model of an STM32 low-power MCU (right).

a resource-constrained tag introduces undesirable complexity. To assess the system's tolerance without compensation, we used simulation to evaluate the maximum tolerable SFO across different message lengths.

We simulated an increasing clock deviation by resampling the envelope signal before adding noise, and tested message lengths of 20, 60, and 100 symbols. Naturally, an SFO integrates over the course of the message, leading to a higher susceptibility of long messages.

As expected, SFO effects accumulate over longer messages, reducing tolerance. Figure 13 (left) shows that decoding remains reliable only for small SFO values: messages with 20 symbols tolerate up to 0.4 % deviation, while longer messages show degraded performance even at lower offsets.

To evaluate whether ultra-low-power MCUs can meet these precision requirements, we measured the supply-voltage-dependent clock frequency of four STM32L073RZ devices [14], repeating each test ten times for consistency. As shown in Figure 13 (right), clock frequency deviates significantly as voltage decreases, reaching up to 2 % at 1.65 V. Additionally, clock frequencies vary by more than 0.8 % between devices, even at the same voltage—well beyond the tolerance of the decoder. This inter-device variability confirms the need for dynamic compensation or SFO-tolerant designs in low-power systems.

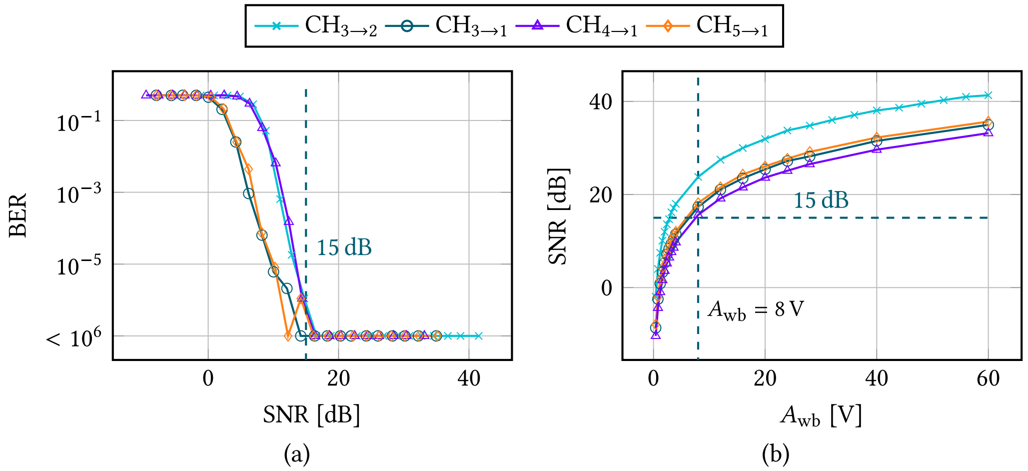

(a)

(b)

Fig. 14. SNR requirements for robust decoding in the simulated channels (a), and the wideband signal peak amplitudes required to achieve a certain SNR at the receiver (b).

4.2.4 Noise Tolerance. To determine the minimum SNR required for reliable decoding, we gradually increased AWGN noise power in the simulation and calculated SNR based on the envelope prior to noise injection. Figure 14(a) shows that BERs exceed 10^{-5} when the SNR drops below 10 dB to 15 dB. In a controlled lab environment, the tag's ADC samples showed a noise standard deviation of 7.3 mV. Maintaining an SNR above 15 dB thus requires a signal standard deviation of at least 41.1 mV. While this is easily achieved in wirelessly powered systems—where signal amplitudes typically exceed several hundred millivolts—it may pose a challenge for semi-passive or active tags operating at longer ranges with reduced channel gains.

Using these SNR thresholds, we estimate the minimum transmit amplitude required for robust communication. Figure 14(b) shows that a peak signal amplitude of just 8 V is sufficient for reliable decoding in all tested channels—simplifying transmitter design. However, this estimate assumes ideal, stationary lab conditions with only AWGN. Real-world deployments may introduce additional noise sources, such as structural vibrations from traffic, that could further impact receiver performance.

5 Prototype Development and Implementation

We implemented a prototype tag to demonstrate the proposed WB-PPM scheme under realistic conditions, using a single transducer for simultaneous wireless power transfer and acoustic communication. This section outlines the prototype's hardware design, describes major integration challenges, and presents the strategies employed to ensure robust synchronization, efficient energy harvesting, and ultra-low-power operation.

5.1 Hardware Architecture

This section describes the major hardware components of the prototype tag. Figure 15 sketches the hardware, consisting of an ultra-low-power microcontroller, an envelope detector, a backscatter modulator, and a harvesting controller. Each block is designed to achieve the targeted sub-milliwatt power consumption while enabling robust communication and simultaneous energy harvesting.

Transducer Selection. In Figure 15, the transducer is represented by its Thevenin equivalent—an ideal voltage source with a series impedance. In our experiments, we selected disk-shaped

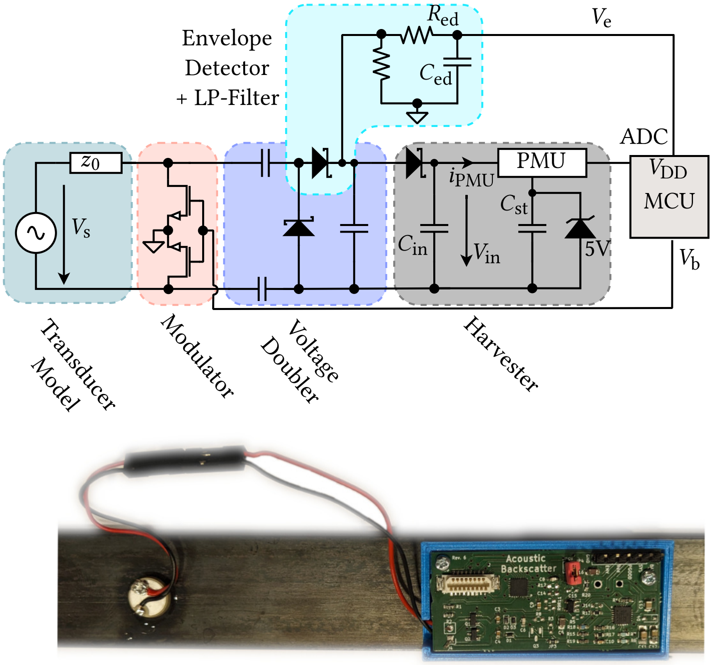

Fig. 15. The tag circuit consists of a modulator, an envelope detector, and a harvester, which supplies the MCU. The transducer is modeled with its Thevenin equivalent. The picture (bottom) shows the full tag prototype on a metal beam.

transducers from PICeramics [21] with 1 cm diameter and 2 mm thickness, resulting in a resonance frequency around 200 kHz. Excitation of the desired Lamb-waves is most effective when the wavelength matches the material thickness. In steel, the resonance frequency results in a wavelength of about 1.4 cm, suitable for common structural elements like H-beams with thicknesses between 1 cm and 2 cm.

Backscatter Modulator. The modulator backscatters signals by toggling between high and low impedance states across the transducer terminals. To handle the differential voltage, we used two N-channel MOSFETs (*SI2302CDS*), chosen for their low on-state resistance (under 0.1 Ω at 1.8 V), allowing direct control from the microcontroller without level shifting. The MOSFETs can withstand drain-source voltages up to 20 V, suitable for our backscatter system.

Voltage Rectification and Envelope Detection. The voltage doubler rectifies and boosts transducer voltage, preparing it for envelope detection. Minimizing the rectifier's output resistance is key to efficient energy harvesting. We used 1 µF series capacitors, yielding an impedance below 0.8 Ω at frequencies above 200 kHz. The *RB751S40* Schottky diode, with a forward voltage drop of 0.28 V and reverse current under 10 nA, balances low voltage drop with minimal leakage [16]. The envelope detector filters the rectified signal. The components C_{ed} and R_{ed} together with the transducer's impedance z_0 form a lowpass filter. Similar to the simulated detector (in Section 4), values are chosen to establish a cutoff frequency close to the symbol rate. The ED has a high input impedance to avoid draining current from the transducer, preserving harvesting efficiency. We selected $R_{ed} = 1.68\,\text{M}\Omega$ and $C_{ed} = 22\,\text{pF}$, resulting in a lowpass cutoff frequency of 4.3 kHz.

Energy Harvesting System. Parallel to the envelope detector, the power management unit (PMU) harvests energy from the rectifier output. We chose the *ADP5091* PMU from *Analog Devices* for its low minimum input voltage (80 mV) and cold-start with just 380 mV. It integrates a switching voltage booster and an MPPT controller that extracts energy from the input capacitor C_{in} and transfers it to the storage capacitor C_{st}. This ensures that the harvester's average input resistance ($V_{\text{in}}/i_{\text{PMU}}$) matches the source's output impedance z_0, thereby optimizing harvesting efficiency. According to the datasheets recommendations, we used a 10 µF input capacitor, and a 200 µF storage capacitor. The PMU is configured with external components to output a regulated 1.8 V supply voltage, which it enables once the storage capacitor voltage exceeds 3.3 V, and disables again when dropping below 1.8 V. Storage capacitor size and voltage thresholds can be adjusted to meet the application's energy requirements, ideally supporting a full duty cycle on a fully charged capacitor. However, larger capacitors are favorable to higher threshold voltages, as leakages increase strongly at higher voltages [19].

Microcontroller Integration. The MCU samples the envelope detector's output and processes the signal digitally. It further controls the modulator to backscatter messages. To run the tag with minimal input power, we chose the ultra-low-power *STM32L031* microcontroller. It features a STOP mode with down to 5 µW power consumption and adaptable clock frequency using an internal low-power oscillator. To minimize power consumption and reduce leakage in the harvester, the supply voltage was set to 1.8 V, as power usage scales quadratically with voltage.

5.2 Design Challenges and Solutions

A real-world prototype introduces several technical challenges. This section discusses the main issues encountered and presents the mitigation strategies developed to maintain communication performance and energy efficiency.

5.2.1 Harvester and Communication Coupling. Using the same transducer for WPT and data transmission is challenging. On the one hand, the data encoding influences the harvested power, inherent to the chosen modulation scheme (cf. Section 3.1). On the other hand, harvester activity distorts the received signal: Commercially available PMUs, including the selected one, are not designed for simultaneous harvesting and communication. This leads to three issues.

(1) The boost regulator requires at least 10 µF capacitance C_{in} for efficient operation [7], which, combined with the large output impedance z_0 of piezoelectric elements, forms a lowpass filter that limits data rates (cutoff frequency at around 15 Hz). Another diode between the voltage doubler and the harvester addresses this effectively, ensuring the ED detects at least the diode's forward voltage drop when V_s rises, while preventing reverse current flow when V_s drops. However, the additional diode reduces overall harvesting efficiency.
(2) The PMU's MPPT feature periodically interrupts harvesting to measure the open-circuit voltage ($i_{\text{PMU}} = 0$), causing abrupt changes in the rectifier voltage, distorting V_e. To prevent this during our experiment, we disabled MPPT and operate on a fixed power point, further reducing efficiency.
(3) When the storage capacitor is charged to its set maximum voltage, the harvester shuts down to prevent damage. This causes a similar sudden voltage spike and potential message distortion. We mitigated this by adding a Zener diode in parallel to the storage capacitor to prevent overcharging.

While these measures reduced efficiency, they were necessary for using an off-the-shelf PMU. Future work should focus on a more integrated solution that gives the MCU finer control over the harvester, maintaining a constant input impedance during message reception and activating MPPT only when no signal is present.

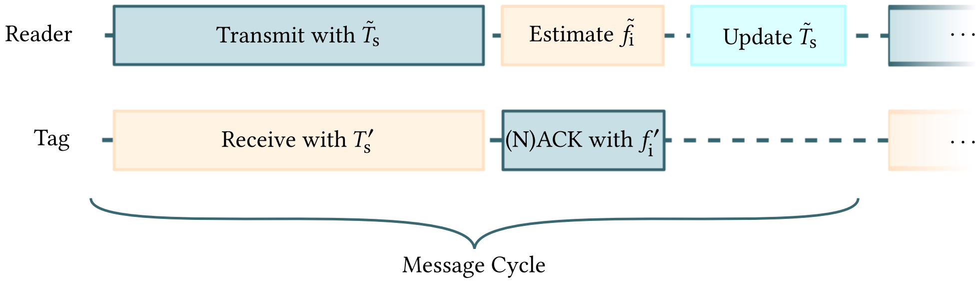

Fig. 16. The reader utilizes an acknowledgment to estimate the tag's sampling clock offset and adapts its symbol interval accordingly in the next message.

5.2.2 *Sample Frequency Offset Mitigation Strategy.*

As shown in Section 4.2.3, ultra-low-power MCUs exhibit SFO, which necessitates dynamic adaption to keep reader and tag synchronized. However, performing SFO detection and correction on the tag is impractical due to strict resource and power constraints. To address this, we shift the responsibility for SFO tracking to the reader, which typically has more computational capacity.

Leveraging the fact that the tag derives its sampling frequency and the intermediate frequency used for backscattering from the same oscillator, we introduce a lightweight protocol in which the tag responds to each received packet with either an Acknowledgment (ACK) or a non-acknowledgement (NACK). The reader uses this feedback to estimate the tag's clock deviation and adjust the symbol duration accordingly for subsequent transmissions. The tag generates its ACK using backscatter modulation at a nominal intermediate frequency f_i. Due to clock deviations, the actual intermediate frequency is f_i'. Similarly, the actual symbol interval T_s' experienced by the tag deviates from the nominal symbol interval T_s. The reader, by analyzing the ACK/NACK packets, infers the intermediate frequency estimate $\tilde{f}_i$. From this, it computes an updated symbol interval $\tilde{T}_s$ to match the tag's timing. The overall estimation and adjustment process is illustrated in Figure 16.

To facilitate robust frequency estimation, the ACK/NACK signals are designed as single-frequency backscatter pulses. The reader processes the received signal by shifting it to baseband, producing the complex signal $y[k]$. It then calculates the average phase shift between consecutive samples:

$$\Delta\phi_i = \measuredangle \left(y[k+1] * y^*[k] \right) . \tag{9}$$

Using this phase shift, the reader estimates the tag's actual intermediate frequency:

$$\tilde{f}_i = f_i + \frac{\Delta\phi_i}{2\pi} \cdot f_s , \tag{10}$$

where f_s is the reader's sampling rate. The updated symbol interval is then computed as

$$\tilde{T}_s = T_s \cdot \frac{f_i}{\tilde{f}_i} . \tag{11}$$

The ACK and NACK are distinguished by the duration of the backscatter pulse: an ACK lasts 20 ms, and a NACK 30 ms. These durations are chosen to exceed the channel's delay spread, minimizing frequency distortion caused by multipath propagation. The performance of this estimation strategy is further evaluated in Section 6.2.2.

5.2.3 *Power Management and Duty Cycling.*

We tailored the tag's firmware to reduce power consumption as much as possible, which is paramount in wirelessly powered devices, e.g., to maximize the turn-on distance. Therefore, we leverage two power-saving options: Reducing the MCU's supply voltage as much as possible, and adapting the clock frequency to be only as fast as required. Therefore, we distinguish between two phases: The charging phase, where the sinusoidal carrier is active, but no message is modulated on the carrier, and the reception phase, where the reader transmits a message. During the charging phase, the MCU scans for the initialization pulse that marks the start of a message. Therefore, the MCU smoothes the samples with an Exponentially-Weighted Moving Average (EWMA) filter. In our tests, a sampling rate of only 1 kHz detected message starts reliably and timely. Therefore, we scaled the MCU clock frequency down to 500 kHz during the charging phase, which was the lowest rate sufficient to process each sample in time.

Upon detection of message initialization, the MCU switches into the reception phase. The required sampling rate for message decoding is higher, and the receiver algorithm in this phase is significantly more complex. Hence, the required clock frequency rises to 4 MHz, and a sampling rate to $N_\mathrm{m}/T_\mathrm{s}$. The MCU then runs the same receiver algorithm we introduced in Section 3.2. After message reception, the MCU generates the ACK/NACK signal for 20 ms, or 30 ms, respectively, and then switches back into the charging phase by reducing the clock frequency and sampling rate.

6 Prototype Evaluation and Experimental Validation

To validate the performance of the prototype tag, we conducted a comprehensive experimental evaluation addressing both communication robustness and energy harvesting efficiency. This evaluation was carried out on the GW channels previously characterized in Section 4.1. Finally, we evaluated power consumption and resulting practical throughput limitations under batteryless operation.

6.1 Setup

To generate signals for wideband downlink communication and receive backscattered acknowledgments, we implemented a software-defined transceiver in Python, reusing code from our simulation study. We employed the TiePie HS-5 USB oscilloscope and signal generator to convert the digital signals into analog form. Both the transmitted and backscattered signals required additional analog processing, which was handled by the analog frontend of a previously developed reader device detailed in [19].

This analog frontend boosts the transmit signal to amplitudes of up to ±14 V, necessary for driving high-impedance piezoelectric transducers. Simultaneously, it captures the backscattered signal by measuring the current through the transducer and performing demodulation to suppress the carrier and isolate the relevant frequency band.

Originally designed for CW signals, the frontend's output range was insufficient for the higher peak voltages required by wideband pulses. To address this, we inserted a 4:1 transformer (Coilcraft WA8351-AL) at the reader's output, achieving voltage peaks of up to ± 56 V. The complete experimental setup is illustrated in Figure 17.

6.2 Communication Performance

This section evaluates the prototype's ability to reliably transmit and receive data across multiple realistic channels. We first measure the maximum achievable data rates and compare them to simulation benchmarks. Then, we analyze the performance of the sample frequency offset (SFO) mitigation strategy under noisy, multipath-affected conditions.

6.2.1 Achievable Data Rates. To isolate the modulation's effect on robustness, we powered the tag with a battery during this evaluation, eliminating communication failures due to insufficient power. Nonetheless, the tag runs with low-power features, i.e., a limited clock rate, to mimic the same conditions as in the wirelessly powered scenario. Table 2 summarizes the parameters used during all experiment runs.

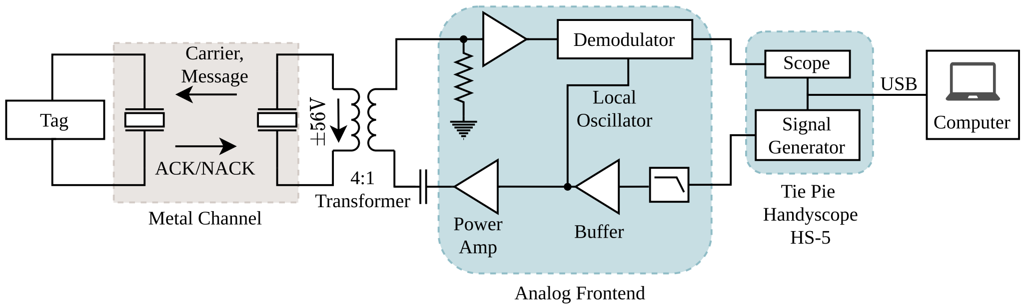

Fig. 17. Experimental evaluation setup: a software-defined transceiver serves as the reader to interrogate the tag. A transformer boosts the output voltage to meet the demands of wideband pulse transmission.

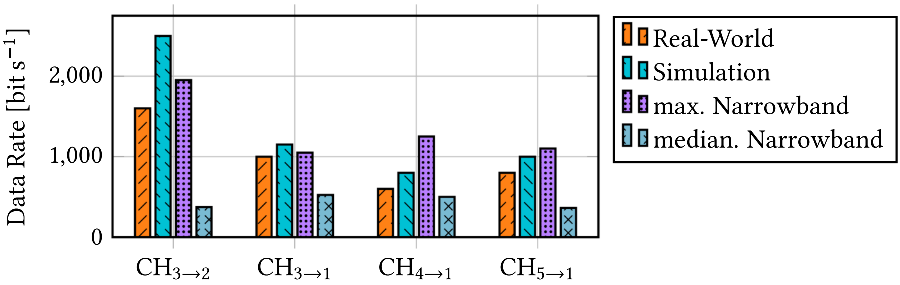

Fig. 18. Data rates achieved with the receiver implementation on MCU compared to achieved data rates from the simulation. The rates of narrowband schemes were only acquired by simulation.

Table 2. Parameters Used During the Experimental Evaluation

Protocol		General	
Transmitted Messages		1,000	
Symbols per Message	N_b	96	
Charging Duration	T_c	80 ms	
Init.-Pulse Duration	T_{off}	4.5 ms	
Symbol Rate	$1/T_s$	100–1600 bit/s	
Modulation		**WB-PPM**	
TX Amplitude	A_{wb}	56 V (peak)	
Bandwidth	B	50 kHz	
Carrier Frequency	f_c	225 kHz	
Receiver		**Synchronization**	**Reception**
Sampling Rate	f_s	1 kHz	N_m/T_s
MCU Clock	f_{MCU}	500 kHz	4 MHz

Figure 18 compares practically achieved and simulated data rates. For every channel and rate, we transmitted 1,000 messages with 96 bits per message. As in the simulation, we assessed a data rate achievable if the BER was below 10^{-5}. During all experiments, the reader applied the SFO estimation technique, adapting the symbol interval dynamically.

We observed lower achievable data rates in real-world tests compared to the simulation results. However, some differences stem from practical limitations: In CH$_{3\rightarrow2}$, communication at 1,600

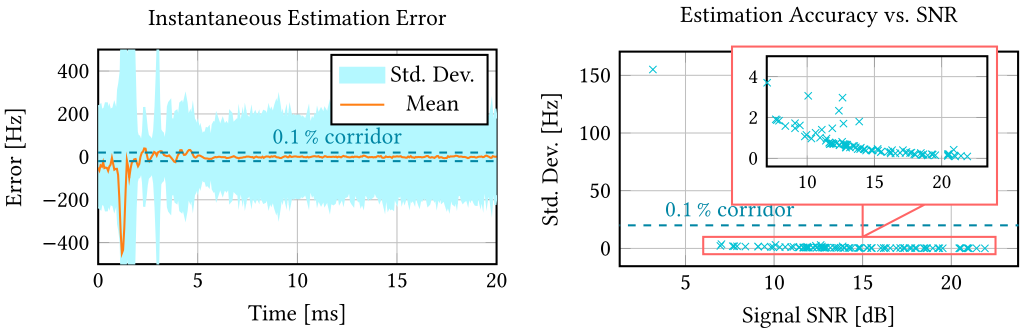

Fig. 19. Accuracy of SFO estimation based on ACK/NACK packets. (Left) Instantaneous estimation error from phase differences between consecutive samples. (Right) Standard deviation of estimates across various SNRs.

bits^{-1} was error-free, but we could not increase data rates because the MCU was not able to process sampling rates higher than 16,000 samples per second. In the other channels, MCU speed was not a limitation, but bit errors occurred already at lower data rates than in the simulation.

The SFO between the reader and the tag likely causes the degraded real-world performance: Although we adapt the symbol interval dynamically, the estimates are never exact, and the actual SFO varies throughout the message. Furthermore, the diode-based envelope detector is not ideal; therefore, its output is distorted compared to the simulation output. During the simulation, we additionally adapted the cutoff frequency of the lowpass filter according to the symbol rate. In the real-world experiment, we used a fixed cutoff frequency for all data rates to avoid manual component resoldering to adapt the analog lowpass filter to different symbol rates. Hence, slightly reduced performance in the real-world experiment is expected.

Despite the reduced throughput, the wideband pulse-based modulation scheme still achieves significantly higher data rates than the 20 bits^{-1} to 200 bits^{-1} reported in previous studies (compare Table 1). A direct comparison with the narrowband modulation schemes is inconclusive. The best schemes at carefully-selected carrier frequencies facilitate higher rates than WB-PPM in real-world tests in all channels. However, those frequencies are usually unknown, and the median narrowband data rate of all frequencies is, in all cases, below the wideband rates. Therefore, the wideband scheme provides more robust and faster communication without adapting the carrier frequency to each channel. Furthermore, the narrowband schemes were only evaluated in simulation and likely face similar degradation under real-world conditions. This supports the usefulness of WB-PPM.

6.2.2 *Sample Frequency Offset.*

Section 4.2.3 showed that our prototype's clock accuracy necessitates an effective SFO mitigation strategy. The approach presented in Section 5.2.2 relies on estimating the $\tilde{f}_\text{i}$ from backscattered ACK/NACK packets. Here, we evaluate the accuracy of this estimation under realistic conditions—including noise and multipath propagation.

Therefore, we applied the estimation algorithm to 9,000 recorded ACK packets, spanning 30 carrier frequencies and three representative SFO values.

Figure 19 (left) shows the instantaneous SFO estimates, derived from phase differences between adjacent samples. During the first few milliseconds of each ACK, multipath transients cause large estimation errors. However, a steady-state emerges after approximately 5 ms, at which point mean estimation error across all ACKs drops below 0.1 % of the carrier frequency—well within the receiver's tolerance, as no decoding errors were observed below this threshold in simulation.

Despite this, the standard deviation of the instantaneous estimates remains high—about 200 Hz—equivalent to an SFO of 2.5 %, far exceeding the system's tolerance. Thus, averaging the instantaneous estimates over the full ACK/NACK package is required.

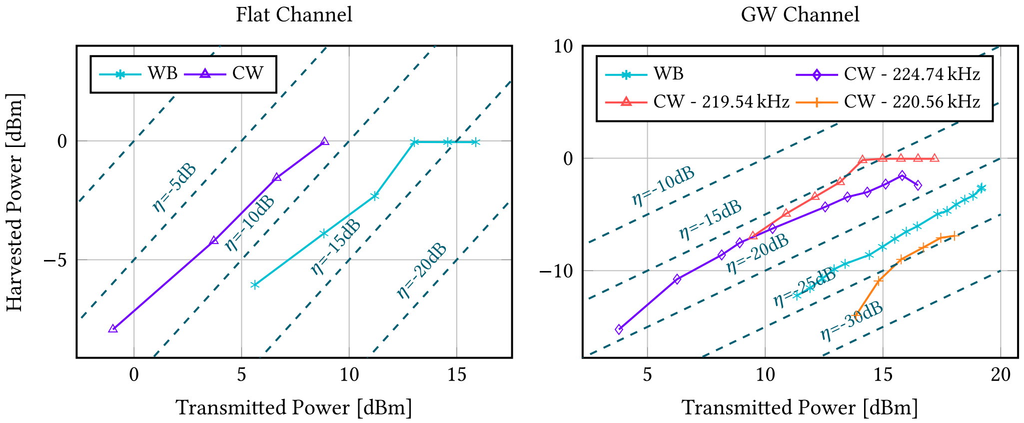

Fig. 20. Power Transfer Efficiency η with wide- and narrowband pulses in an ideal flat channel (left) and in a real GW channel, where the carrier frequency is important (right).

To improve robustness, we discard the first 5 ms of each ACK average the remaining instantaneous estimates. As shown in Figure 19 (right), averaging significantly reduces the variability. At SNRs as low as 7 dB, the standard deviation of the resulting estimates remains below 2 Hz in most cases, corresponding to a tolerable clock mismatch of just 0.025 %. Only one notable outlier occurred at a carrier frequency with an SNR of 3 dB, where the error increased to approximately 155 Hz. In such cases, further refinement—such as averaging across multiple ACKs—may be required to ensure reliability. However, such low SNRs are rarely observed. Nevertheless, these extreme conditions are rare. Under typical operating scenarios, the proposed estimation method provides sufficient accuracy to compensate for sampling frequency offsets at the reader.

6.3 Power Transfer Efficiency

Besides communication performance, the tag's energy harvesting capability is critical for sustained operation. This section examines the power transfer efficiency of wideband versus narrowband signals. We measured the harvested power at the harvester's regulated output, incorporating losses from the channel, rectifier, PMU, and leakages. Therefore, we placed a 3.3 kΩ resistance at the 1.8 V output and measured the duty cycle of the harvester. The transmitted power was derived from current and voltage measurements at the TX transducer. From the average TX power and the average available power, we obtained efficiency η.

Figure 20 (left) shows the transfer efficiency in an ideally flat channel. Therefore, we placed an 1 kΩ resistor between reader and tag, emulating a source with fixed output impedance typical in through-metal channels. WPT with CW achieved an efficiency of roughly −7 dB. At the same time, the efficiency using wideband pulses was about −12.7 dB—only a quarter of the CW efficiency. As the idealized channel is frequency-flat, i.e., the waveform's frequency spectrum does not influence channel losses, the drop in efficiency must be attributed to the selected harvester circuit, which seems to work better with CW than WB signals.

When repeating the same experiment on a real GW channel, the carrier frequency has a significant impact. We first chose two frequencies with a high voltage gain on the specimen: 219.54 kHz and 224.74 kHz. We then compared these to wideband pulses. The results are shown in Figure 20 (right). In the real channel, all efficiencies are lower than in the flat channel, with roughly −15 dB for the best CW frequency. The difference between the wideband pulses and the best CW frequencies increased to about −7.5 dB. However, the WB pulses perform better than a CW frequency with a

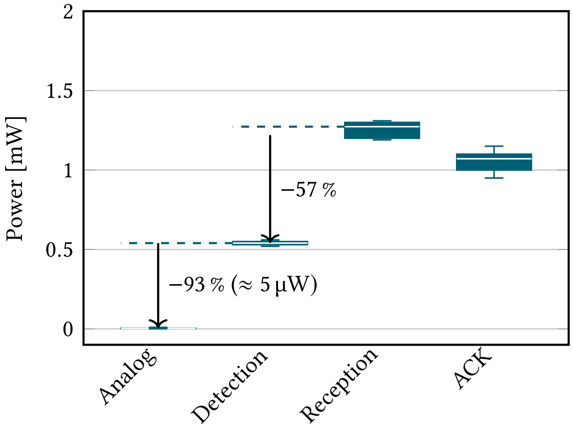

Fig. 21. Power Consumption of the MCU during its three states while receiving a packet with $T_s = 1\,\text{ms}$ and $N_b = 96$, and during STOP mode with analog detection. Each boxplot shows the distribution of power measurements during the state.

medium voltage gain, e.g., 220.56 kHz. Ultimately, when choosing a frequency with a particularly low voltage gain, the power was insufficient to charge the harvester. Hence, no efficiency could be measured.

These results demonstrate that most efficient power transfer requires choosing a suitable CW frequency. Furthermore, we can expect to harvest about 5 to 6 times less power during downlink communication with wideband-modulated messages compared to narrowband modulation. However, wideband power transfer may still be useful during tag discovery—when the reader does not yet know suitable frequencies for each tag—or when multiple tags must be supplied at the same time: Every tag has a different frequency response, and carrier frequencies suitable for all tags may not exist.

6.4 System-level Throughput with Energy Constraints

Achieving high data rates in batteryless systems not only depends on communication robustness but also on the balance between harvested and consumed energy. In this section, we model the maximum sustainable data rates considering the prototype's measured power consumption and harvesting efficiency. Different frame synchronization strategies are evaluated to highlight the tradeoffs between power conservation and effective throughput.

Section 6.2.1 considered the maximum achievable data rates for error-free decoding. However, available power also limits the effective data rates in productive batteryless systems. During message reception, the tag has (1) a higher power consumption because the receiver algorithm demands a higher clock rate, and (2) harvests less power from the modulated downlink signal compared to the CW charging waveform. Hence, the tag must store enough energy to sustain operation during message reception, and between messages, it may require time to charge before the following message starts. To estimate the maximum effective data rate, we acquire the MCU's power consumption throughout the message cycle.

MCU consumption measurements were done with supply voltage of 1.8 V. Figure 21 shows the consumption during detection, reception, and acknowledgment generation. Message reception is the most demanding state with up to 1.2 mW power consumption, followed by acknowledgment generation. During the charging phases, the MCU remains in detection, actively trying to detect the start of the next downlink message. Here, reducing the clock frequency during the packet detection phase saves about 57 % power compared to keeping the same clock rate in all states.

Enabling the tag to continuously listen requires harvested power to exceed the detection-mode consumption, making further power reduction in that mode desirable. While we did not implement it in our prototype, analog detectors, creating a digital bitline for the microcontroller as shown in Figure 2 seem promising for message detection. Therefore, we include an analog detector in the following analysis, assuming the MCU can remain in STOP mode, where it only consumes 5 µW, waiting for an external interrupt from the analog detector to signal a new message. The analog detector itself can be implemented with nanopower comparators, not adding significant power consumption to the circuit.

We estimate the maximum achievable data rates when taking the charging and ACK phases into account, assuming that the reader transmits a message as soon as the tag has charged sufficiently to receive it. These rates must be seen as an upper bound and are not practically achievable. Without knowing the tag's state of charge, the reader will either transmit too early, risking packet loss, or too late, not utilizing the maximum potential rate.

In our model, we denote the durations the tag spends in the states *charging and detection*, *reception*, and *acknowledgment* as $t_\mathrm{c}, t_\mathrm{r}$, and t_a. Similarly, $P^\mathrm{c}_\mathrm{c}, P^\mathrm{c}_\mathrm{r}$, and P^c_a are the consumed powers in each state, and $P^\mathrm{h}_\mathrm{c}, P^\mathrm{h}_\mathrm{r}$, and P^h_a are the harvested powers per state. During continuous maximum-rate communication, the tag must harvest at least as much energy as it consumes throughout message reception. Hence,

$$t_\mathrm{c}\left(P^\mathrm{h}_\mathrm{c} - P^\mathrm{c}_\mathrm{c}\right) + t_\mathrm{r}\left(P^\mathrm{h}_\mathrm{r} - P^\mathrm{c}_\mathrm{r}\right) + t_\mathrm{a}\left(P^\mathrm{h}_\mathrm{a} - P^\mathrm{c}_\mathrm{a}\right) \geq 0\,. \tag{12}$$

This equation yields the minimum charge time between messages

$$t_\mathrm{c} \geq \frac{-t_\mathrm{r}(P^\mathrm{h}_\mathrm{r} - P^\mathrm{c}_\mathrm{r}) - t_\mathrm{a}(P^\mathrm{h}_\mathrm{a} - P^\mathrm{c}_\mathrm{a})}{P^\mathrm{h}_\mathrm{a} - P^\mathrm{c}_\mathrm{a}}\,. \tag{13}$$

The consumed powers have been measured in Figure 21. Furthermore, we assume that $P^\mathrm{h}_\mathrm{a} = 0.5P^\mathrm{h}_\mathrm{c}$ because the transducer is short-circuited half the time while transmitting the acknowledgment. From Section 6.3, we assume $P^\mathrm{h}_\mathrm{r} \approx 0.2P^\mathrm{h}_\mathrm{c}$. Then, we derive the maximum rate as

$$R = \frac{N_\mathrm{b}}{t_\mathrm{c} + t_\mathrm{r} + t_\mathrm{a}} \quad \text{with} \quad t_\mathrm{r} = T_\mathrm{off} + (7 + N_\mathrm{b})T_\mathrm{s}\,, \tag{14}$$

with N_b payload bits, and a 7-symbol preamble. Acknowledgments are 20 ms long.

Figure 22 shows the maximum rates for the different frame synchronization implementations depending on the harvested power. Two methods rely on the MCU to sample and detect an initialization pulse, once with full MCU speed and once with reduced speed, as implemented in our prototype. The third method assumes an analog detector, so that the MCU can remain in the power-conserving stop mode during the charging phase. The model demonstrates that reduced power consumption during detection reduces the minimum harvested power required to charge the tag, hence, enabled longer power-transfer distances reduced charging durations. Furthermore, an analog detector enables significantly higher effective data rates when the harvested power is low. In fact, in the low-power regime, the charging durations have a higher impact on the effective data rate than the symbol duration. Only when harvested power exceeds a certain threshold, in this example about 4 mW, the tag harvests more than it consumes in all states. Hence, nothing is gained by further reducing power consumption.

Our evaluation demonstrates that the prototype sustains robust wideband communication and energy harvesting despite real-world imperfections. Energy-aware design choices are essential for maximizing throughput, confirming the practicality of WB-PPM for low-power through-metal applications.

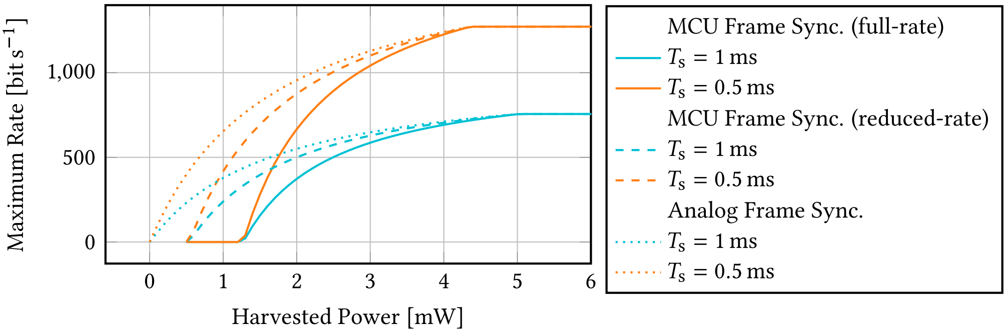

Fig. 22. The maximum effective data rate of a batteryless tag when using frame synchronization with full MCU speed, reduced MCU speed, and analogously with the MCU in stop-mode. The messages were $N_b = 96$ bits long with a symbol rate of $1/T_s$.

7 Discussion

This work demonstrates that energy harvesting and signal reception on a shared transducer inherently interfere with each other—posing a significant design challenge for acoustic sensing in metal environments. Prior studies have addressed this coupling through various strategies.

One straightforward solution is to equip the tag with two separate transducers—one dedicated to energy harvesting and the other to communication [1]. This decouples the harvester's current draw from the downlink signal and prevents backscatter modulation from affecting the harvested power. However, this approach increases component cost, occupies more physical space, and complicates deployment—particularly in embedded or space-constrained scenarios.

An alternative, frequency-division approach was proposed in [4], where power and data signals are transmitted at distinct carrier frequencies. At the tag, passive bandpass and bandstop filters are used to isolate the two paths. However, both piezoelectric transducers and the GW metal channels exhibit narrowband resonance, and achieving adequate frequency separation requires high-order, high-Q filters—which are complex to design and often prohibitively expensive.

A third strategy, used in conventional RFID and underwater backscatter systems, relies on a fixed-impedance harvester [12, 22]. This configuration extracts a nearly constant current from the transducer throughout the downlink phase, typically by matching the transducer impedance to that of the load. While effective in RF and underwater applications, this method is inefficient in GW metal channels due to the strongly frequency-selective transducer impedance. Instead, we advocate for a harvester equipped with MPPT, supplemented by fine-grained control from the MCU: During message reception, MPPT sampling may be temporarily suspended to prevent interference with decoding.

Because acoustic WPT is inefficient, minimizing tag power consumption is essential for achieving acceptable operating ranges at practical transmit power levels. In our microcontroller-based implementation, the MCU is the dominant energy consumer, drawing between 500 µW and 1.2 mW during active operation—on average consistent with our sub-milliwatt target. To ensure immediate readiness upon startup, the tag remains in a low-power detection mode with a power threshold below 0, dBm—well within the achievable range of a 1 W commercial reader in guided metal structures.

These results align with comparable systems. For instance, WISP consumes approximately 850 µW[22], and the underwater tag described in [12] operates at roughly 500 µW, despite relying on analog demodulation techniques. Although custom integrated circuits can reduce power consumption by up to 20 times [31], their high development costs make them viable only for large-scale deployments involving thousands of nodes. For smaller deployments or research prototypes, MCU-based tags provide an accessible and cost-effective alternative for embedding sensors in metallic environments.

8 Conclusion

Wirelessly powered sensors integrated into civil infrastructure or industrial facilities have a large potential to reduce maintenance costs. Acoustic communication and power transfer are beneficial whenever sensors are shielded by metal. Conventional techniques for downlink communication to such passive sensors—as known from RFID—are strongly limited in data rate because of the guided wave channel's large delay spread. This work investigated wideband pulses to increase the robustness against multipath propagation as an alternative to commonly used continuous wave modulation schemes. We tested the proposed scheme in simulation and validated it with a custom-designed prototype. Achievable data rates with conventional schemes were shown to depend strongly on the carrier frequency. Without prior channel knowledge, the average achievable data rate of wideband pulse-position modulation was about 2.3 times higher than continuous wave modulation.

Sampling clock offsets, which are common in wireless communication, prevent correct decoding. As tags are typically resource-constrained, we designed a clock offset detection and mitigation scheme that works solely on the reader, which has significantly more computational resources. In our experiments, the reader could successfully detect and compensate for clock deviations of more than 1 %, which are typical for ultra-low-power microcontrollers.

Analysis of the prototype revealed that simultaneous harvesting and communicating via the same transducer introduces a severe challenge. To overcome this, the MCU on the tag requires more fine-grained control over the state of the harvester. Furthermore, an investigation of the potential of wideband pulses for WPT has shown that the harvester circuit loses roughly 5 dB in efficiency when using wideband pulses. However, without prior knowledge about suitable carrier frequencies, wideband pulses are a comparable alternative to continuous wave signals for power transfer.

Analysis of the power consumption and harvesting potential has shown that reducing the tag's idle power consumption significantly affects tag availability and effective data rate. This hints at potential improvements by integrating an analog circuit to detect the start of a message, allowing the tag's MCU to remain in a power-saving mode until a message starts.

References

[1] Sayed Saad Afzal, Waleed Akbar, Osvy Rodriguez, Mario Doumet, Unsoo Ha, Reza Ghaffarivardavagh, and Fadel Adib. 2022. Battery-free wireless imaging of underwater environments. *Nature Communications* 13, 1 (2022), 5546–5554. DOI: https://doi.org/10.1038/s41467-022-33223-x

[2] Daniel Arnitz, Ulrich Muehlmann, and Klaus Witrisal. 2012. Characterization and modeling of UHF RFID channels for ranging and localization. *IEEE Transactions on Antennas and Propagation* 60, 5 (2012), 2491–2501. DOI: https://doi.org/10.1109/TAP.2012.2189705

[3] Jonathan D. Ashdown, Kyle R. Wilt, Tristan J. Lawry, Gary J. Saulnier, David A. Shoudy, Henry A. Scarton, and Andrew J. Gavens. 2013. A full-duplex ultrasonic through-wall communication and power delivery system. *IEEE Transactions on Ultrasonics, Ferroelectrics, and Frequency Control* 60, 3 (2013), 587–595. DOI: 10.1109/TUFFC.2013.2600

[4] Ananya Bhardwaj, Ahmed Allam, Alper Erturk, and Karim G. Sabra. 2023. Ultrasound-powered wireless underwater acoustic identification tags for backscatter communication. *IEEE Transactions on Ultrasonics, Ferroelectrics, and Frequency Control* 71, 2 (2023), 1–1. DOI: https://doi.org/10.1109/TUFFC.2023.3344638

[5] Soumya Chakraborty, Gary J. Saulnier, Kyle W. Wilt, Edward Curt, Henry A. Scarton, and Robert B. Litman. 2015. Low-power, low-rate ultrasonic communications system transmitting axially along a cylindrical pipe using transverse waves. *IEEE Transactions on Ultrasonics, Ferroelectrics, and Frequency Control* 62, 10 (2015), 1788–1796. DOI: 10.1109/TUFFC.2015.007078

[6] Bruno Clerckx, Junghoon Kim, Kae Won Choi, and Dong In Kim. 2022. Foundations of wireless information and power transfer: Theory, prototypes, and experiments. *Proc. IEEE* 110, 1 (2022), 8–30. DOI: https://doi.org/10.1109/JPROC.2021.3132369

[7] Analog Devices. 2016. ADP5091/ADP5092 Datasheet. Retrieved April 23, 2025 from https://www.analog.com/media/en/technical-documentation/data-sheets/ADP5091-5092.pdf

[8] Lianghui Ding, Kehong Chen, Falong Huang, Feng Yang, and Liang Qian. 2020. Modeling and evaluation of piezoelectric transducer (PZT)-based through-metal energy and data transfer. *MDPI Sensors* 20, 11, Article Number 3304 (2020). DOI: https://doi.org/10.3390/s20113304

[9] EPCglobal. 2018. EPC Radio-Frequency Identity Protocols Generation-2 UHF RFID Standard. Retrieved April 23, 2025 from https://www.gs1.org/standards/rfid/uhf-air-interface-protocol

[10] Bundesministerium für Digitales und Verkehr. 2022. Verkehrsinvestitionsbericht für das Berichtsjahr 2020. Retrieved April 23, 2025 from https://bmdv.bund.de/goto?id=513572

[11] Raffaele Guida, Neil Dave, Francesco Restuccia, Emrecan Demirors, and Tommaso Melodia. 2019. U-Verse: A miniaturized platform for end-to-end closed-loop implantable internet of medical things systems. In *Proceedings of the 17th Conference on Embedded Networked Sensor Systems*. ACM. DOI: https://doi.org/10.1145/3356250.3360026

[12] Junsu Jang and Fadel Adib. 2019. Underwater backscatter networking. In *Proceedings of the ACM Special Interest Group on Data Communication*. ACM. DOI: https://doi.org/10.1145/3341302.3342091

[13] Tristan J. Lawry, Kyle R. Wilt, Jon D. Ashdown, Henry A. Scarton, and Gary J. Saulnier. 2013. A high-performance ultrasonic system for the simultaneous transmission of data and power through solid metal barriers. *IEEE Transactions on Ultrasonics, Ferroelectrics, and Frequency Control* 60, 1 (2013), 194–203. DOI: https://doi.org/10.1109/TUFFC.2013.2550

[14] ST Microelectronics. 2022. STM32L073RZ Datasheet. Retrieved April 23, 2025 from https://www.st.com/resource/en/datasheet/stm32l073rz.pdf

[15] Rito Mijarez and Patrick Gaydecki. 2013. Automatic guided wave PPM communication system for potential SHM of flooding members in sub-sea oilrigs. *Smart Materials and Structures* 22, 5 (2013), 55031–55039. DOI: https://doi.org/10.1088/0964-1726/22/5/055031

[16] Ziping Cao Ming Yuan and Jun Luo. 2018. Characterization the influences of diodes to piezoelectric energy harvester. *International Journal of Smart and Nano Materials* 9, 3 (2018), 151–166. DOI: https://doi.org/10.1080/19475411.2018.1454532

[17] Adam B. Noel, Abderrazak Abdaoui, Tarek Elfouly, Mohamed Hossam Ahmed, Ahmed Badawy, and Mohamed S. Shehata. 2017. Structural health monitoring using wireless sensor networks: A comprehensive survey. *IEEE Communications Surveys and Tutorials* 19, 3 (2017), 1403–1423.

[18] Peter Oppermann and Bernd-Christian Renner. 2022. Equalization for high-bitrate acoustic backscatter communication in metals. In *Proceedings of the 2022 International Conference on Embedded Wireless Systems and Networks*. ACM. Retrieved from http://hdl.handle.net/11420/13283

[19] Peter Oppermann and Bernd-Christian Renner. 2023. Acoustic backscatter communication and power transfer for batteryless wireless sensors. *MDPI Sensors* 23, 7, Article number 3617 (2023). DOI: https://doi.org/10.3390/s23073617

[20] Peter Oppermann and Christian Renner. 2022. Higher-order modulation for acoustic backscatter communication in metals. In *Proceedings of the ACM SIGCOMM 2022*. DOI: https://doi.org/10.1145/3544216.3544261

[21] PI Ceramics. 2023. Piezoelektrische Scheiben. Retrieved April 23, 2025 from https://www.piceramic.de/fileadmin/user_upload/physik_instrumente/files/datasheets/PRYY-Datenblatt.pdf

[22] Alanson P. Sample and Joshua R. Smith. 2013. The wireless identification and sensing platform. *Wirelessly Powered Sensor Networks and Computational RFID* (2013), 33–56. DOI: https://doi.org/10.1007/978-1-4419-6166-2_3

[23] Sameer M. Shaik, Xinyao Tang, and Soumyajit Mandal. 2020. Self-optimizing wireless networks on structures. *IEEE Transactions on Circuits and Systems II: Express Briefs* 67, 5 (2020). DOI: https://doi.org/10.1109/TCSII.2020.2983931

[24] D. A. Shoudy, G. J. Saulnier, H. A. Scarton, P. K. Das, S. Roa-Prada, J. D. Ashdown, and A. J. Gavens. 2007. P3F-5 an ultrasonic through-wall communication system with power harvesting. In *Proceedings of the 2007 IEEE Ultrasonics Symposium Proceedings*. DOI: https://doi.org/10.1109/ULTSYM.2007.465

[25] Fabian Steinmetz and Bernd-Christian Renner. 2021. From the long-range channel in the ocean to the short-range and very shallow-water acoustic channel in ports and harbors. In *Proceedings of the 2021 5th Underwater Communications and Networking Conference*. IEEE. DOI: https://doi.org/10.1109/UComms50339.2021.9598094

[26] Zhongqing Su. 2009. *Identification of Damage Using Lamb Waves : From Fundamentals to Applications*. Springer. DOI: https://doi.org/10.1007/978-1-84882-784-4

[27] Yongshun Sun, Yunfei Xu, Wei Li, Quanchang Li, Xiaoxi Ding, and Wenbin Huang. 2021. A lamb waves based ultrasonic system for the simultaneous data communication, defect inspection, and power transmission. *IEEE Transactions on Ultrasonics, Ferroelectrics, and Frequency Control* 68, 10 (2021), 3192–3203. DOI: https://doi.org/10.1109/TUFFC.2021.3087603

[28] Xinyao Tang, Soumyajit Mandal, and Tayfun Özdemir. 2022. A CMOS SoC for wireless ultrasonic power/data transfer and SHM measurements on structures. *IEEE Access* 10 (2022), 110163–110180. DOI: https://doi.org/10.1109/ACCESS.2022.3214231

[29] Yunfei Xu, Yongshun Sun, Jian Tang, Chao Wei, Xiaoxi Ding, and Wenbin Huang. 2022. A lamb waves-based wireless power transmission system for powering IoT sensor nodes. *Smart Materials and Structures* 31, 10 (2022), 105009–105019. DOI: https://doi.org/10.1088/1361-665X/ac8ada

[30] Ding-Xin Yang, Zheng Hu, Hong Zhao, Hai-Feng Hu, Yun-Zhe Sun, and Bao-Jian Hou. 2015. Through-metal-wall power delivery and data transmission for enclosed sensors: A review. *MDPI Sensors* 15, 12 (2015), 31581–31605. DOI: https://doi.org/10.3390/s151229870

[31] Daniel Yeager, Fan Zhang, Azin Zarrasvand, Nicole George, Thomas Daniel, and Brian Otis. 2013. SOCWISP: A 9 μA, addressable gen2 sensor tag for biosignal acquisition. *Wirelessly Powered Sensor Networks and Computational RFID* (2013), 57–78. DOI: https://doi.org/10.1007/978-1-4419-6166-2_4

A Open-source Publication

To enable other researchers to reproduce our results or use the same conditions to test other modulation schemes, we publish the code of the simulation as an easy-to-use and easy-to-extend python module. It also includes the channel impulse responses of the recorded channels. Both can be found in a Git repository hosted at https://collaborating.tuhh.de/e-24/public/acoustic-backscatter/downlinkSimulation.

Furthermore, we also publish the schematics, PCB layout, and Firmware of the tag prototype in a second Repository located at https://collaborating.tuhh.de/e-24/public/acoustic-backscatter/backscattertag. Lastly, the reader device that was used in the experimental evaluation of our tag, is also part of an open source release. Its schematics can be found at https://collaborating.tuhh.de/e-24/public/acoustic-backscatter/backscatterreader.

Received 26 February 2024; revised 23 June 2025; accepted 29 June 2025